# Design of an Ultra-High-Speed Permanent-Magnet Motor for an Electric Turbocharger Considering Speed Response Characteristics

Myung-Seop Lim, Ji-Min Kim, Yong-Suk Hwang, and Jung-Pyo Hong, *Senior Member, IEEE*

***Abstract*—This paper presents a design methodology and analysis for a 4-kW 150-krpm ultra-high-speed surface-mounted permanent-magnet synchronous motor (SPMSM) to electrically assist a turbocharger. The proposed design methodology is aimed at achieving a required torque and speed. In addition, this study seeks a fast-speed response as a design objective to eliminate turbo lag more effectively. First, an existing prototype that does not meet the target performance is presented. The loss for the prototype, which is difficult to obtain theoretically, is obtained experimentally and reflected in the design. The speed response characteristic of the machine is analyzed through the electromechanical undamped natural frequency and damping ratio. Design parameters such as the permanent-magnet (PM) grade, the turn number of coils, and the axial length of the motor are designed. The resulting improved motor achieves higher power density as well as faster speed response than the prototype. Experiments verified the effectiveness of the motor in the electrically assisted turbocharger. In system experiments with the turbocharger, the rising speed of the boost pressure is improved by 44.9% due to the designed motor.**

***Index Terms*—Power density, speed response, surface-mounted permanent-magnet synchronous motor (SPMSM), turbocharger, ultra-high-speed motor.**

## I. Introduction

TURBOCHARGERS are typically implemented in engine systems as a technological step toward engine downsizing. In a conventional turbocharger, the turbine is driven by the exhaust gas coming from the engine cylinder, and air is supercharged into the inlet in the engine cylinder while the impeller connected to the turbine is rotated. A contributing factor to the degradation of vehicle performance is the turbo lag caused by low engine revolutions per minute (rpm). A low-engine rpm results in a low discharge rate of the exhaust gas, and a correspondingly low rotational speed of the turbine, which reduces the supercharging capacity of the impeller [1], [2]. To reduce this turbo lag, and thus improve the engine performance and vehicle drivability, a turbocharger system assisted by an ultra-high-speed electric motor with high-speed response is developed. Fig. 1 shows the block diagram of the electrically assisted turbocharger.

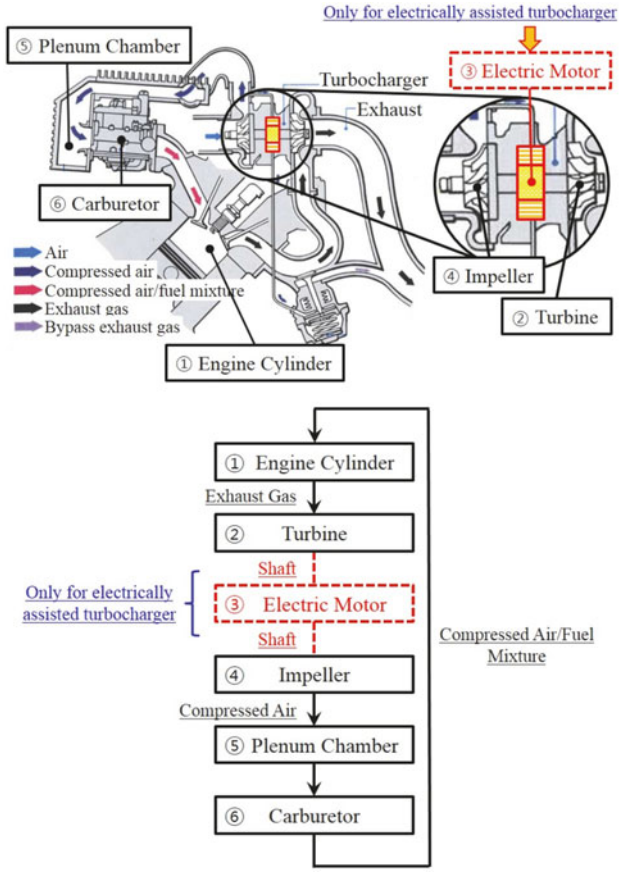


Fig. 1. Block diagram of an electrically assisted turbocharger.

Manuscript received January 25, 2016; revised May 5, 2016, August 4, 2016, and October 10, 2016; accepted November 29, 2016. Date of publication December 1, 2016; date of current version April 14, 2017. Recommended by Technical Editor S. K. Dwivedi. This work was supported by the Ministry of Science, ICT, and Future Planning (MSIP), Korea, under the Information Technology Research Center (ITRC) supported program (IITP-2016-H8601-16-1005) supervised by the Institute for Information and Communications Technology Promotion (IITP).

The authors are with Department of Automotive Engineering, Hanyang University, Seoul 04763, Korea (e-mail: limmang87@hanyang.ac.kr; kimjm567@hanyang.ac.kr; ryanhwang@hanyang.ac.kr; hongjp@hanyang.ac.kr).

Color versions of one or more of the figures in this paper are available online at http://ieeexplore.ieee.org.

Digital Object Identifier 10.1109/TMECH.2016.2634160

1083-4435 © 2016 IEEE. Personal use is permitted, but republication/redistribution requires IEEE permission.
See http://www.ieee.org/publications_standards/publications/rights/index.html for more information.

Among ultra-high-speed compact motors, permanent-magnet (PM) machines are considered favorites. Their high power densities lead to high-speed system response [3]. Furthermore, nonelectric excitation in the rotors yields excellent efficiency [4]. The ultra-high-speed operation and increased power density, however, have led to both electrical and mechanical issues such as iron loss, voltage limitation, windage loss, and structural problems [5]. In addition, as the speed response of the motor increases, the impeller reaches the rated speed sooner, which indicates that the turbo lag removal performance is improved. Accordingly, fulfilling the required specifications and speed response characteristics are significant issues in the design of ultra-high-speed machines.

Research addressing the typical design specifications and methodology of high-speed PM motors for turbochargers, taking into account the speed response characteristic and power density, is sparse. In addition, it is difficult to find prior research on the actual effectiveness of electrically assisted turbochargers. Although research has been performed in the area of ultra-high-speed motors for turbocharger systems, induction machines (IMs) or synchronous reluctance machines (SRMs) with relatively lower power density than that for PM motors have been presented [6]–[8]. Designs for PM motors with speeds of up to 10–75 krpm in applications such as compressors and pumps have been described [9]–[14]. However, the previous research [6]–[14] does not discuss the speed response of the machines, or the usability or effectiveness of the motors in turbochargers. The design process for a motor with the same base speed and maximum speed as the target specifications has been studied [15]; however, electromagnetic design issues for high-speed motors, such as the number of poles/slots and the shape of the iron core, are emphasized. In this paper, the speed response characteristics and effectiveness of the motor in the turbocharger are analyzed; in addition, the target torque is increased so that the outer diameter of the stator and the input current are larger than those of the existing prototype.

This paper discusses an ultra-high-speed surface-mounted permanent-magnet synchronous motor (SPMSM) for electrically assisted turbochargers, which can reduce turbo lag presented under start/stop conditions as well as during gear changes. The result is improved vehicle performance and higher overall system efficiency [6]. It is not common for automobiles to have specifications for high-speed motors that reach speeds ranging from 100 000 to 150 000 rpm. In addition, there are parameters that are difficult to calculate theoretically in the design of high-speed motors. In particular, the motor for a turbocharger requires significant design experience, even in the thermal aspect, since it comes in contact with the engine, a complex mechanical structure, and it is affected by the driving patterns. As a result, the specifications and design methodology presented in this paper include design experience or experimental approaches.

This study proposes a design methodology for the 4-kW 150-krpm SPMSM based on an existing prototype. The input voltage of the designed motor and the prototype are the same. In addition, all machine parts mounted with the motor, including the cooling system and turbocharger itself, are the same. They were not directly designed; those developed and manufactured by the automobile company are used. Since the shape design methodology of the stator teeth and yoke is the same as in a previous study [15], it has been omitted from this paper. Instead, this study mainly deals with the power density and speed response of the high-speed motor, as well as its effectiveness in the turbocharger. In the proposed methodology, the appropriate PM grade is selected and the design parameters—such as series turn number per phase and axial length—are analyzed. The values of the parameters are determined while considering the electromechanical undamped natural frequency and the damping ratio obtained from the transfer function of the system. Meanwhile, the iron and mechanical losses have particularly significant effects on the target performance of the ultra-high-speed machine. Windage loss is caused by the friction of the rotor and shaft with the surrounding air, and the bearing loss is the friction loss that occurs in the bearing between the shaft and the housing. These losses are small enough to be ignored at low speeds. However, they have a tendency to become significant as the speed increases; therefore, they cannot be ignored in ultra-high-speed systems. In this regard, the accurate estimation of these mechanical losses is required for precise design and performance prediction. Thus, mechanical losses such as windage or bearing losses are obtained via experimental methods using the existing prototype in the turbocharger. The iron loss map according to the armature current of 0–180 $A_{rms}$ and speed of 0–150 krpm is obtained using a nonlinear finite element method (FEM). As a result of this design, both the power density and the speed response of the motor were improved. The performance of the designed motor that successfully fulfills the requirements was verified experimentally. In addition, this paper presents the effectiveness of the designed motor in the turbocharger system via the experiments. In the experiments, the boost pressure in the electrically assisted turbocharger was examined. The boost pressure exerted by the motor in the electrically assisted turbocharger was compared with that of a conventional turbocharger system.

The two main contributions of this paper are as follows: First, the design methodology of a motor for a turbocharger that considers the speed response is developed. A fast-speed response of the motor and the system is essential to effectively reduce turbo lag in the turbocharger. A transfer function that includes all electrical/mechanical parameters is obtained based on the numerical model of the motor. Based on this function, the speed response due to a change in design variables was analyzed and reflected in the design. In addition, losses such as windage loss and bearing loss that should be taken into account when designing a high-speed motor were obtained through experimental evaluation using an existing prototype and reflected as a mechanical loss in the design. Second, a confirmation of the performance of the turbocharger mounted with the designed motor is obtained. The performance of the turbocharger mounted with the motor is compared with that of the conventional turbocharger. The objective is to verify the efficacy of the designed motor and improve its performance beyond that of the conventional turbocharger by manufacturing and testing the electrically assisted turbocharger using the ultra-high-speed motor designed using the method proposed in the first main contribution.

TABLE I
SPECIFICATION OF THE PROTOTYPE AND REQUIREMENTS

| Quantity | Unit | Prototype | Requirement |
|---|---|---|---|
| Supply voltage | $V_{dc}$ | | 48 |
| Current limit | $A_{rms}$ | | 180 |
| Outer diameter | mm | | 90 |
| Power | kW | 3.5 | 4 |
| Rated torque | N·m | 0.38 | 0.38 |
| Rated speed | rpm | 87,500 | 100,000 |
| Max. speed | rpm | - | 150,000 |
| Axial length | mm | 20 | under 20 |
| Response time (80 krpm) | ms | 297.93 | under 297.93 |

## II. ANALYSIS OF THE PROTOTYPE

The prototype that was developed by an automotive company does not meet the required specifications of Table I. The purpose of the design in this study is to improve the power density and speed response of the motor, which are mutually independent design objectives. The proposed prototype meets the specifications shown in Table I. The rated power and speed of the improved motor should achieve 4 kW and 100 krpm, and the motor should be able to reach a maximum speed of 150 krpm. In addition, the design objectives are to minimize the axial length for improved power density and response time of the motor. Thus, analysis of the prototype is a basis for the formulation of the improved design plan.

### A. Prototype

The prototype is a two-pole six-slot SPMSM with concentrated windings. The diameter of the stator and rotor are 90 and 23 mm, respectively. The stack length is 20 mm. A parallel magnetized $Sm_2Co_{17}$ PM was used for the rotor. For the prototype, a ring-type magnet of two poles was used. This means that in the cylindrical shape of the magnet, one half has an N-pole, while the other has an S-pole. In addition, the surface of the rotor was surrounded by a retaining sleeve to prevent the scattering of the cylindrical PM by the centrifugal force. For the armature winding, there were 14 series turns per phase and one parallel circuit. As a result, the back electromotive force (BEMF) of the prototype at a 10 krpm rotational speed was approximately 1.31 $V_{rms}$. Accordingly, voltage saturation occurs at 87 500 rpm as a result of high BEMF, and it cannot reach the rated speed of 100 000 rpm when driven by the $I_d = 0$ control method.

### B. Mechanical Loss

The mechanical loss consisted of both windage and bearing losses as the experimental results of the prototype were used to design the improved motor. This is because the mechanical components of the improved motor—such as the shaft, bearing, and turbocharger—were the same as those of the prototype. The experimental setup for the no-load torque test is shown in Fig. 2(a). The shaft and bearing are used in the same manner as those used in the actual turbocharger. In the place of an impeller, a cylindrical dummy was installed in the impeller position inside the turbocharger. The mass of the dummy is the same as that of the impeller. The air flow channel in front of the dummy is closed

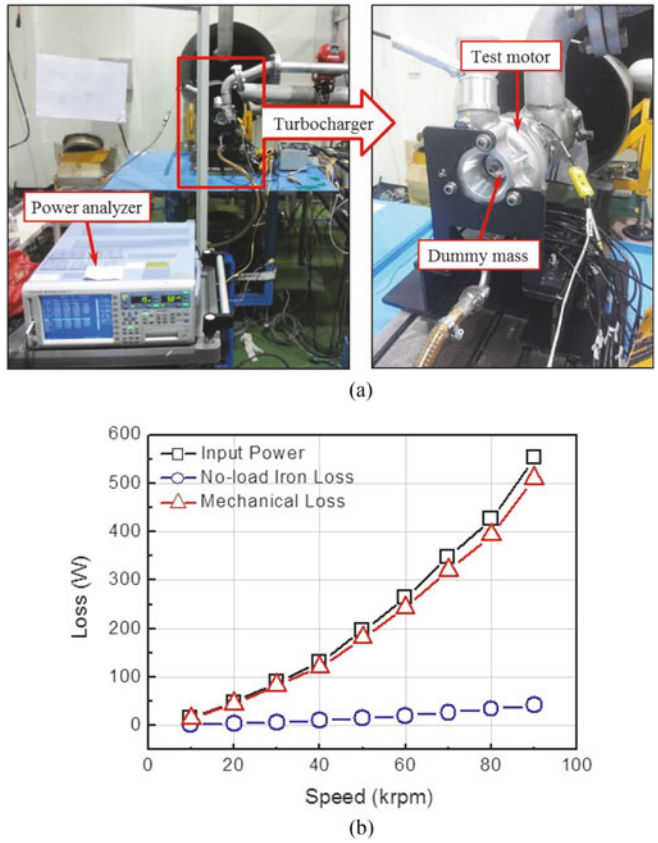


Fig. 2. No-load test of the prototype. (a) Experimental setup. (b) Mechanical loss as the test result.

by a cap. Through this process, it is possible for the motor be in a no-load condition by suppressing the load due to air. Thus, the input power indicated the sum of the mechanical loss and a no-load iron loss. The copper loss can be disregarded because the square of the input current was extremely small under the no-load condition. Consequently, the mechanical loss is calculated by subtracting the no-load iron loss from the input power. The iron loss was obtained via a nonlinear FEM. As a result, the load torque generated by the impeller can be excluded, and the mechanical loss, which is the sum of the windage loss that occurs in the shaft and rotor of the motor, and the friction loss that occur in the bearing, can be obtained. Fig. 2(b) shows the examined losses and the mechanical loss as the no-load test result.

### C. Design Objectives and Parameters

The BEMF of the prototype 1.31 $V_{rms}$ was too large to reach the rated speed of 100 krpm. This is because the voltage was saturated by the BEMF and impedance voltage at approximately 90 krpm. However, if the magnitude of the BEMF is reduced too much, the motor will not achieve the rated torque of 0.38 N·m under 180 $A_{rms}$. Therefore, the appropriate BEMF should be determined so as to fulfill the required specifications. Additionally, the proposed design methodology focuses on the improvement of the speed response characteristic of the machine. Hence, the critical design goals of the proposed methodology are to fulfill the required specifications by

increasing the power density and to achieve fast-speed response to reach the rated speed and power.

In this study, the thickness of the PM was fixed at 5 mm. Outer and inner retaining sleeves were set at 1.5 and 2.5 mm, respectively. They were determined experimentally by considering both the diameter of the shaft and mechanical strength rated by the manufacturer. Thus, the characteristics of the motor can be determined by the PM grade, series turn number per phase $N_{\rm ph}$ and axial length $L$ of the rotor. The PM grade, the series turn number per phase, and the axial length were determined to be the design parameters used to achieve the specified design goals.

## III. Speed Response Characteristics of the Motor

The design methodology based on the mathematical model of an electric motor is proposed to analyze the speed response characteristics. For the proposed methodology, the transfer function of the machine is deduced and the two objective functions representing the speed response characteristic are derived. Finally, the values of the design parameters are determined based on the derived objective functions.

### A. Motor Model in Laplace Domain

A mathematical model was used to analyze the speed response characteristics of electric motors. Motor systems can be expressed by using both electrical and mechanical equations. These are the voltage and torque equations, respectively. The voltage equation of the motor is obtained from a three-phase equivalent circuit, where the iron loss is ignored [16]. The voltage equation of the electric motor is expressed as

$$\begin{aligned} V_a &= R_a i_a + L_a \frac{di_a}{dt} + e_a \\ &= R_a i_a + L_a \frac{di_a}{dt} + k_e \phi_f \omega_m \end{aligned} \tag{1}$$

where $V_a$ and $i_a$ are the armature voltage and current; $R_a$ and $L_a$ are the armature coil resistance and inductance; $e_a$ is BEMF in rms; $k_e$ and $\phi_f$ are the BEMF constant and field flux, respectively; and $\omega_m$ is the mechanical speeds in $\mathrm{rad/s}$. The torque equation is as follows:

$$\begin{aligned} T_e &= J \frac{d\omega_m}{dt} + B\omega_m + T_L \\ &= k_T \phi_f i_a \end{aligned} \tag{2}$$

where $J$ and $B$ are the mass moment of inertia and the friction coefficient, respectively; $T_e$ and $k_T$ are the electric torque and torque constant, respectively; and $\omega_m$ and $T_L$ are the mechanical speeds in rad/s and the load torque, respectively. It was assumed that the load torque $T_L$ is zero and can be neglected in the following equations.

The Laplace transformation of (1) and (2) are computed to obtain the transfer function of the machine in the Laplace domain. The resulting voltage equation is as follows:

$$\begin{aligned} V_a(s) &= (R_a + sL_a) i_a(s) + e_a(s) \\ &= (R_a + sL_a) i_a(s) + k_e \phi_f \omega_m(s). \end{aligned} \tag{3}$$

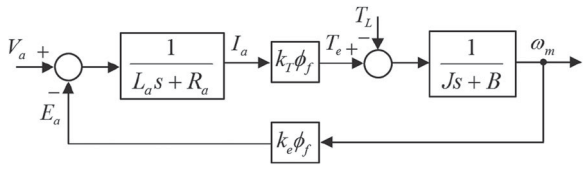


Fig. 3. Block diagram of an electric motor.

The torque equation is expressed as

$$\begin{aligned} T_e(s) &= (sJ + B)\omega_m(s) \\ &= k_T \phi_f i_a(s). \end{aligned} \tag{4}$$

Based on (3) and (4), a block diagram and transfer function can be obtained.

### B. Transfer Function

The block diagram of an electric motor is shown in Fig. 3. From the diagram, the transfer function in the Laplace domain is obtained

$$\frac{\omega_m}{V_a} = \frac{\frac{1}{sL_a + R_a} \cdot k_T \phi_f \cdot \frac{1}{sJ + B}}{1 + \left(\frac{1}{sL_a + R_a} \cdot k_T \phi_f \cdot \frac{1}{sJ + B}\right) \cdot k_e \phi_f}. \tag{5}$$

Equation (5) can be organized in second-order standard form as

$$\frac{\omega_m}{V_a} = \frac{\frac{K}{JL_a}}{s^2 + \left(\frac{R_a}{L_a} + \frac{B}{J}\right) s + \left(\frac{R_a}{L_a} \cdot \frac{B}{J} + \frac{K^2}{JL_a}\right)} \tag{6}$$

where

$$k_e \phi_f = k_T \phi_f = K. \tag{7}$$

From (6) and (7), the electromechanical undamped natural frequency $\omega_n$ and damping ratio $\zeta$ are obtained as

$$\omega_n = \sqrt{\frac{B}{J} \cdot \frac{R_a}{L_a} + \frac{K^2}{JL_a}} \tag{8}$$

$$\zeta = \frac{1}{2\omega_n} \left(\frac{B}{J} + \frac{R_a}{L_a}\right). \tag{9}$$

The high electromechanical undamped natural frequency $\omega_n$ and low damping ratio $\zeta$ can lead to fast response speeds in electric machines [17]. Therefore, $\omega_n$ and $\zeta$ are used as the objective functions to estimate the speed response characteristic.

In the presented equations, $K$ is proportional to both the series turn number per phase $N_{\rm ph}$ and axial length $L$. The mass moment of inertia $J$ is proportional to the axial length $L$, and inductance $L_a$ is proportional to $L$ as well as the square of $N_{\rm ph}$. Consequently, assuming that the friction coefficient $B$ is extremely small or zero, $\omega_n$ is constant under the condition of the same BEMF or torque constant. Therefore, with the constant $\omega_n$, $\zeta$ should be minimized to achieve a fast response speed in the machine [17]. However, there are practical limitations in the determination of $N_{\rm ph}$ due to the current density in the armature coil. Hence, the values of $N_{\rm ph}$ and $L$ for the improved motor

should be determined by considering both the speed response and the appropriate current density.

## IV. Improved Design and Verification

The power density of the motor can be increased through forced air cooling using a fan, water cooling, or oil cooling, because these methods increase the current density of the motor. However, this method requires a new cooling system or mechanism to improve the cooling performance, thereby increasing the overall cost, complexity, and volume of the system. An alternate method is to use cobalt steel instead of silicon steel as the core material, because the magnetic properties of cobalt steel is much better than those of silicon steel. However, processing the cobalt steel is relatively difficult and expensive. Alternatively, the motor type can be changed to improve the torque density at the same current. For example, an interior permanent-magnet synchronous motor (IPMSM), which has saliency, has relatively higher torque density because of the usage of the reluctance torque. However, IPMSM is more vulnerable to stress and is more structurally unstable compared to the SPMSM adopting the retaining sleeve because of the presence of a rib or air barrier in the rotor. Therefore, to improve the power density of the motor, the PM material was selected as one of the design parameters. Residual induction and coercive force of the PM material were taken into consideration. After determining the PM material, the series turn number per phase $N_{\rm ph}$ and axial length $L$ were designed to improve the speed response. The tendency of the speed response characteristic, according to the variations of $N_{\rm ph}$ and $L$, were analyzed using the equations in Section III. Finally, the values of the parameters for the improved motor were determined to achieve both high power density and faster response speeds. The core iron shape of the stator affects the saturation and iron loss, which, in turn, affect the performance of the motor. However, the shape design methodology of the stator teeth and yoke in this study is the same as the process in [15] and has been omitted from this paper. Thus, the design steps are as follows.

1) The grade of PM is determined in accordance with the operating temperature and cooling system.
2) Based on the proposed mathematical model, the trajectory of the damping ratio on changes in axial length and series turn number per phase is obtained.
3) The series turn number per phase is determined on the basis of the current density.
4) The axial length of the motor is determined based on the trajectory.
5) The performance of the motor designed by reflecting the losses is analyzed and verified experimentally.

### A. Permanent Magnet

The $Sm_2Co_{17}$ magnet used in the prototype has high heat resistance and strong temperature characteristics. Thus, it is suitable for use in environments with very high temperatures. However, the maximum temperature of the PM in the rotor was estimated experimentally to be approximately 100 °C in the turbocharger. This is because the PM of the motor is not in direct contact with the exhaust gas in the turbocharger. The temperature of the PM is affected by the shaft, which is connected by heat conduction to the turbine and impeller. Furthermore, the turbocharger is applied with an oil cooling system to decrease the temperature. In addition, $Sm_2Co_{17}$ magnets are more expensive than NdFeB magnets even though they have lower mechanical strength and residual induction than those of NdFeB magnets.

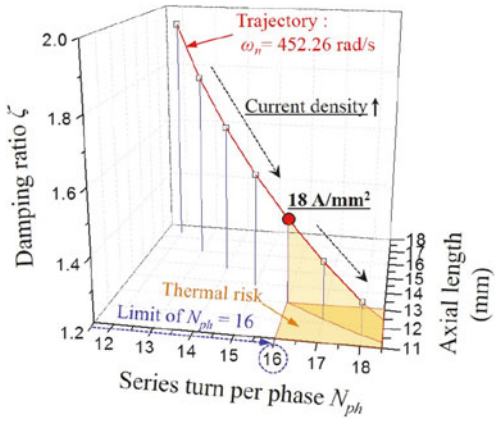


Fig. 4. Trajectory of the damping ratio according to the series turn number per phase and axial length.

At 100 °C, residual induction of the $Sm_2Co_{17}$ is 1.051 T. On the other hand, residual induction of the N38EH, which is one of the NdFeB magnets, is 1.149 T. Noting that irreversible demagnetization under full-load conditions should be avoided, an N38EH with a high coercive force was determined to be appropriate for the application. Its coercive force was 756 kA/m and its intrinsic coercive force was over 2400 kA/m. For these reasons, the N38EH—which is one of the NdFeB magnets—was adopted for the design of the improved motor.

To maximize the power density, the width of the PM should be maximized. In addition, for the case of a high-speed motor, the number of poles should be minimized because of the limitation of carrier frequency [18]. Accordingly, two poles as the minimum number of poles are used in this study. As a result, the ring-type cylindrical magnet itself is used as a rotor to make the utmost use of the PM in the rotor with two poles and to maximize the rotor stiffness. Consequently, the shape of the PM is not considered as a design parameter. In addition, a cylindrical-type retaining sleeve was inserted into the surface inside and outside the PM in the design. As the thickness of the retaining sleeve is greater, it is difficult to increase the power density of the motor. However, this is essential in order to prevent the scattering of the PM due to the vibration and centrifugal force during high-speed operation. Since the thickness of the retaining sleeve of the existing prototype is the value determined experimentally, the internal and external sleeves of the same thickness and material are used in the improved motor. Therefore, it can be stated that the effect of the magnet material on the power density is 9.3% as a rate of increase in the residual induction of the PM.

### B. Series Turn Number per Phase

Fig. 4 shows the trajectory of the damping ratio $\zeta$ under the constant $\omega_n$ condition. The trajectory is obtained using (8)

and (9) from Section III, and the assumption that the friction coefficient $B$ is either extremely small or zero. For the trajectory, $\omega_n$ is determined as the maximum BEMF to fulfill both the required specifications and the voltage limitation. If the motor resistance is linear proportional to the axial length $L$, $\zeta$ is proportional to $1/N_{\rm ph}$ and independent from $L$, when $\omega_n$ is constant. Therefore, this cannot explain the relationship between $L$ and $\zeta$ shown in Fig. 4. However, the resistance of the motor is not linear proportional to $L$. If a coil is actually wound, there exists a coil part wound in the axial direction to fall out of one slot and then turn away to go back to the next slot in addition to the coil part that passes through the core through the slot of the motor. This is called an "end turn." These parts are not in proportion to $L$ of the motor. Thus, in effect, resistance is not linear proportional to $L$, and this is particularly true with the thin-type motor dealt with in this paper. Actually, in this study, the effects by $L$ and end turn were all calculated and reflected when the resistance of the motor was calculated. As shown in Fig. 4, a fast-speed response can be attained as a result of the high $N_{\rm ph}$ and short $L$ under the condition of a constant BEMF or torque constant. Therefore, $N_{\rm ph}$ should be as high as possible, considering the current density in the armature coil, to achieve fast-speed responses.

Although the maximum input current and the stator outer diameter of the motor have been determined, the current density can be changed depending on the driving pattern of the system, performance of the cooling system, and contacted mechanical structures. Thus, a numerical approach is difficult since there are too many factors that affect the current density, and nonlinearity is strong. In Fig. 4, $N_{\rm ph}$ and axial length have an infinite degree of freedom. However, if $N_{\rm ph}$ is increased within the predetermined outer diameter, the current density inevitably increases. This is because even if $N_{\rm ph}$ is increased, the slot area cannot be increased due to the magnetic saturation of the core material. As a result, there is a limit in increasing $N_{\rm ph}$ in the design of the actual motor. Therefore, $N_{\rm ph}$ is determined as 16 based on the outer diameter and the current density specified by the designer.

The current density was determined experimentally using the prototype and [19], rather than from a thermal analysis. This is because it is difficult to obtain a reliable thermal analysis result in consideration of the complex structure of the contacted mechanical parts. Consequently, $N_{\rm ph}$ of the improved motor was determined to be 16, since the current density proposed in this study was 18 A/ mm$^2$. A current density of 18 A/ mm$^2$ is a higher value compared to that of conventional continuous ratings with air cooling. There are two reasons for the feasibility of the high current density. First, the motor in the turbocharger is operated intermittently for no more than a few seconds. The continuous operation time of the motor varies significantly depending on the amount of rapid acceleration and subsequent gear shifting. Accounting for the time when the motor reaches the rated speed in the turbocharger, the continuous operation time of the motor can be assumed to be less than 1 to 2 s under normal driving conditions, and it can be assumed to be about seven seconds when a rapid acceleration is maintained while continuously shifting gear. This is because the motor is only operating to eliminate turbo lag when the vehicle is accelerating at low speeds or during gear shifting. Otherwise, the motor is idling or generating using the high-speed exhaust gas. Second, the stator can be cooled indirectly by the cooling oil, which is circulated in the engine and turbocharger system. For these reasons, the series turn number per phase of 16 and the current density of 18 A/ mm$^2$ have been determined to be appropriate values in this application. The effect of the change in current density on the design can be represented numerically by calculating the ratio of the series turn per phase. Consequently, the degree of effect in the improved design becomes 14.3%.

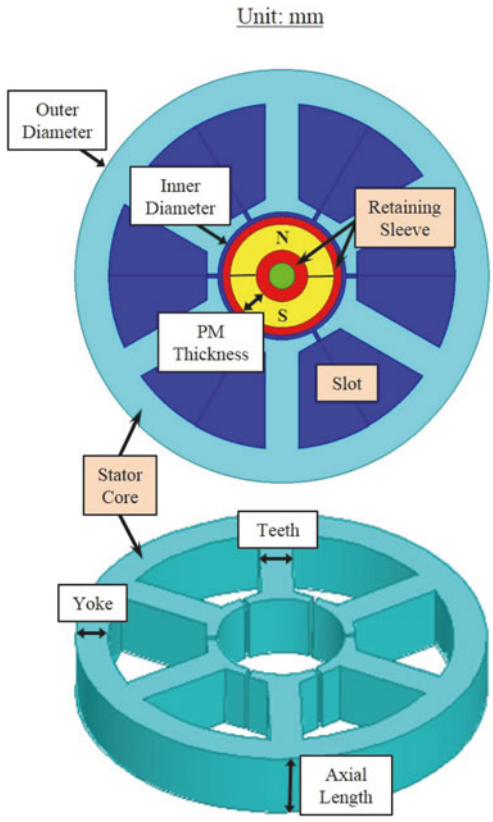


Fig. 5. Configuration of the proposed motors.

## C. Axial Length

Based on the $\zeta$ trajectory, as shown in Fig. 4, the axial length $L$ of the motor was determined to be 13 mm, taking into consideration the magnitude of the BEMF and the series turn number per phase $N_{\rm ph}$. This value is a decrease of 35% compared to 20 mm of the prototype. The BEMF of the improved motor under no-load conditions is obtained via the nonlinear FEM. As the results demonstrate, the BEMF at 10 krpm was 1.09 $V_{\rm rms}$. This is a decrease of about 16.8% compared to the 1.31 $V_{\rm rms}$ of the prototype. The configurations and dimensions of the prototype and improved motor are shown in Fig. 5 and Table II. The effect of the axial length is a 35.0%, a rate of decrease in the length. Further, given the changes in BEMF, it is found that the effect caused by the change in shape of the stator core is 2.5%. A photograph of the designed motor is presented in Fig. 6.

TABLE II
DIMENSIONS OF THE PROTOTYPE AND IMPROVED MOTOR

| Quantity | Unit | Prototype | Improved |
|---|---|---|---|
| Stator outer diameter | mm | 90 | |
| Stator inner diameter | mm | 27.90 | |
| PM thickness | mm | 5.65 | |
| Yoke | mm | 7.85 | 7.30 |
| Teeth | mm | 6.75 | 7.10 |
| Axial length | mm | 20 | 13 |

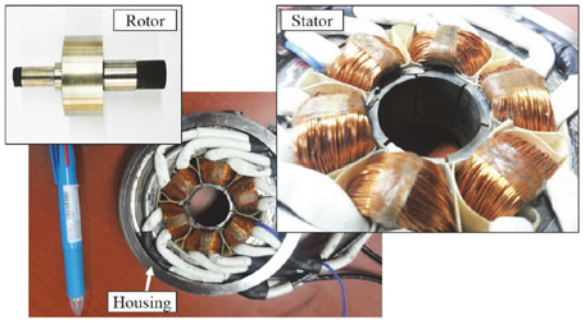


Fig. 6. Improved motor.

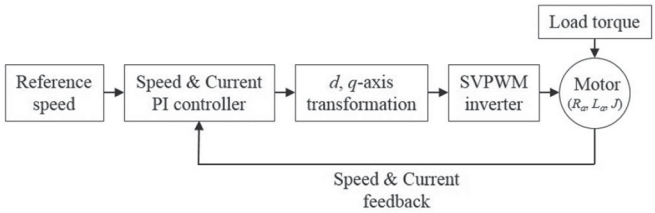


Fig. 7. Block diagram of the MATLAB Simulink model.

## D. Speed Response

The speed response curves for the motors were simulated using MATLAB Simulink. For the simulation, in addition to the motor, the inverter and the controller were modeled, and PI control on the speed and current has been performed, as shown in Fig. 7. The simulation was conducted accounting for the electrical variables of the motor, such as the resistance and inductance, as well as the mechanical variables of mass moments of inertia $J$. The carrier frequency of the space vector pulsewidth modulation (SVPWM) in the inverter model is 20 kHz. Fig. 8 shows the speed response curves of both the prototype and improved motor in reaching the rated power. The times to reach the same speed of 80 krpm for the prototype and the improved motor were 297.93 and 193.47 ms, respectively. Therefore, the speed response of the improved motor is 35.1% faster than that of the prototype due to the proposed design methodology. The design results show that the axial length of the improved motor is reduced by 35% compared to that of the initial prototype, which implies that $J$ of the rotor is reduced by 35%. This accounts for most of the reduction rate of 35.1% in the response time. Therefore, this result indicates that the mechanical parameter $J$ has a stronger effect on the speed response compared with the

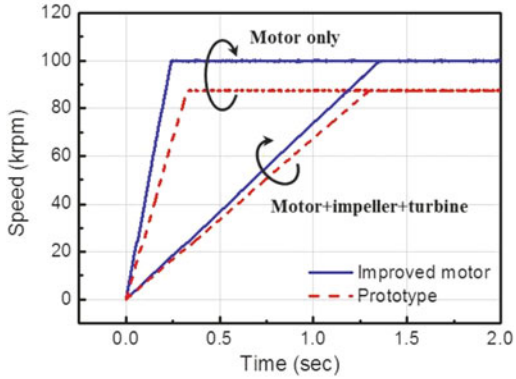


Fig. 8. Speed response of the motors up to reach the rated power.

electrical parameters $R$ and $L$. When the mass moment of inertia of the impeller and turbine are considered, the speed response of the improved motor is 8.62% faster than that of the prototype.

The purpose of this study is to design a fast-speed response that satisfies the target torque and power. Consequently, although $J$ has a dominant influence on the speed response of the motor, a reduction in $J$ leads to a decrease in magnitude of BEMF and in turn makes it impossible to achieve the target performance. If $L$ is decreased by 35%, BEMF is also reduced by 35%, making the magnitude of BEMF 0.98 V, which is less than 1.09 V, and this is unable to satisfy the target torque and power. The results of this study showed that $L$ was minimized in order to reduce $J$, as well as the torque and power were maximized through an appropriate material selection and determination of $N_{\rm ph}$ in order to minimize $L$. Therefore, there is a need to reduce $J$ and implement an appropriate material selection and electromagnetic design to achieve the fast-speed response while satisfying the torque and power.

## E. Motor Characteristics

The $d$-, $q$-axis equivalent circuit is used to simulate the performance of the designed motor with regard to factors such as torque, speed, and armature current [20], [21]. This is different from the three phase equivalent circuit described in Section III. In the $d$-, $q$-axis circuit, the iron loss of the motor is taken into account. This is because the iron loss seriously affects the torque-current performance of the machines at ultrahigh speeds. Subscripts of $d$ and $q$ refer to the $d$- and $q$-axis components; $i$ and $v$ are the armature current and voltage, respectively; $R_a$ is the phase resistance; $R_c$ is the equivalent resistance of the iron loss; $L$ is inductance; $\psi_a$ is the flux linkage of the PM in rms; and $\omega$ is the electrical speed in $\mathrm{rad}/s$. To solve the equivalent circuit, the flux linkage, the inductance, and the iron loss are obtained via a nonlinear FEM. The flux linkage and the $d$-, $q$-axis inductance according to the armature currents of 0–180 $\mathrm{A_{rms}}$ are shown in Fig. 9(a) and (b), respectively. The saturation of the core causes decreases as well as discrepancies between the $d$- and $q$-axis inductances as the armature current increases. Fig. 9(c) shows the iron loss map according to the armature currents of 0–180 $\mathrm{A_{rms}}$ and speeds of 0–150 krpm. The phase angle of the

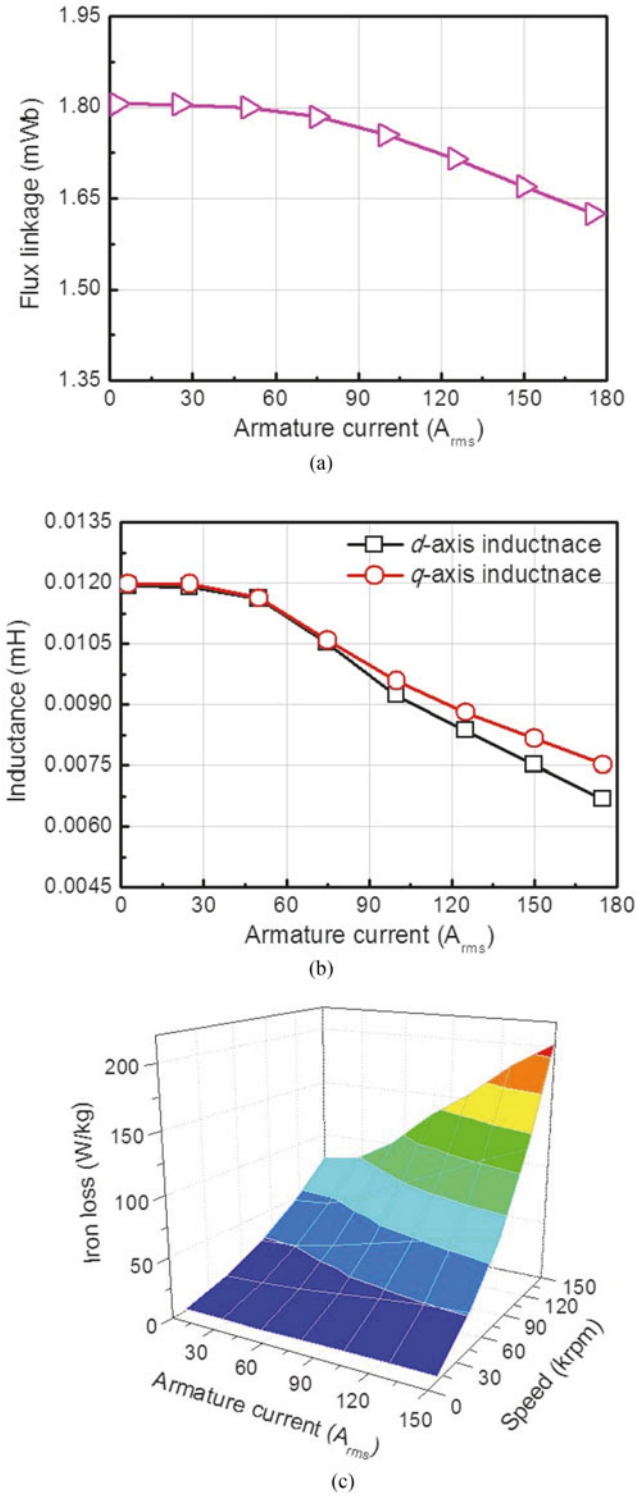


Fig. 9. Variations of the parameters under load conditions. (a) Flux linkage $\psi_a$. (b) *d*-, *q*-axis inductance. (c) Iron loss.

armature current was fixed at 0° because the designed motor is driven by $i_d = 0$ control.

The designed SPMSM was set up, and the experiment was conducted to verify the validity of the proposed design methodology and results. For the test, a torque sensor was located between the two identically designed motors to connect them in

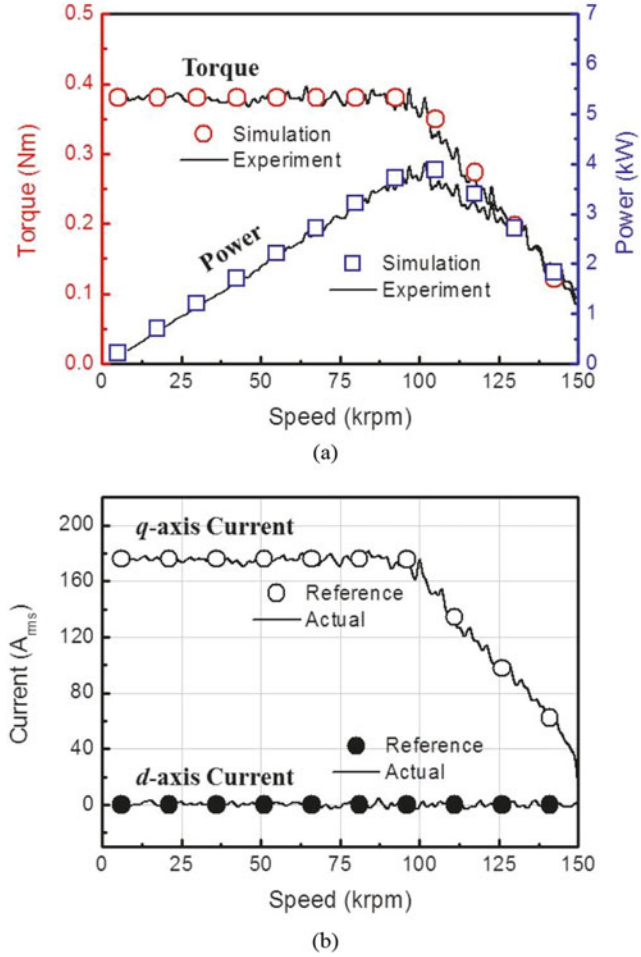


Fig. 10. Load test results of the improved motor. (a) Torque and power. (b) *d*-, *q*-axis input current.

a series. Of the two motors, one was used as a load unit through the torque control, and the other was used as a test motor through the speed control. The test motor was driven by $i_d = 0$ control. The carrier frequency of the controller was 20 kHz during operation, and the iron loss, depending on the magnitude and phase of the input current, was accounted for in control. The details of the inverter and controller are shown in [22]. An SETech YD–series torque sensor and a Yokogawa WT3000 power analyzer were used. Fig. 10(a) shows the torque and power according to the speed. The motor was able to operate at maximum torque until it reached the rated speed of 100 krpm and the output power reached 4 kW. Over the base speed, the motor operated at maximum speed while decreasing torque and power. The input currents under the load conditions are shown in Fig. 10(b). The *d*-axis current was consistently zero because the motor was driven by $I_d = 0$ control. The *q*-axis current was decreased after the base speed such as the torque to maintain the induced voltage. Therefore, the motor can operate to a maximum speed of 150 krpm. The specifications of the designed motor that fulfill the necessary requirements are displayed in Table III. The volume of the designed model relative to the prototype decreased by 35.0%, the rated power and speed increased by 14.3%, and the speed response of the motor increased by 35.1%.

TABLE III
SPECIFICATIONS OF THE DESIGNED MOTOR

| Quantity | Unit | Value | Versus Prototype |
|---|---|---|---|
| Power | kW | 4 | +14.3% |
| Torque | N·m | 0.38 | – |
| Rated speed | rpm | 100,000 | +14.3% |
| Max. speed | rpm | 150,000 | – |
| Outer diameter | mm | 90 | – |
| Axial length | mm | 13 | −35.0% |
| Core material | – | 20PNF1500 | – |
| Magnet material | – | Nd-Fe-B | – |
| Response time (80 krpm) | ms | 193.47 | −35.1% |

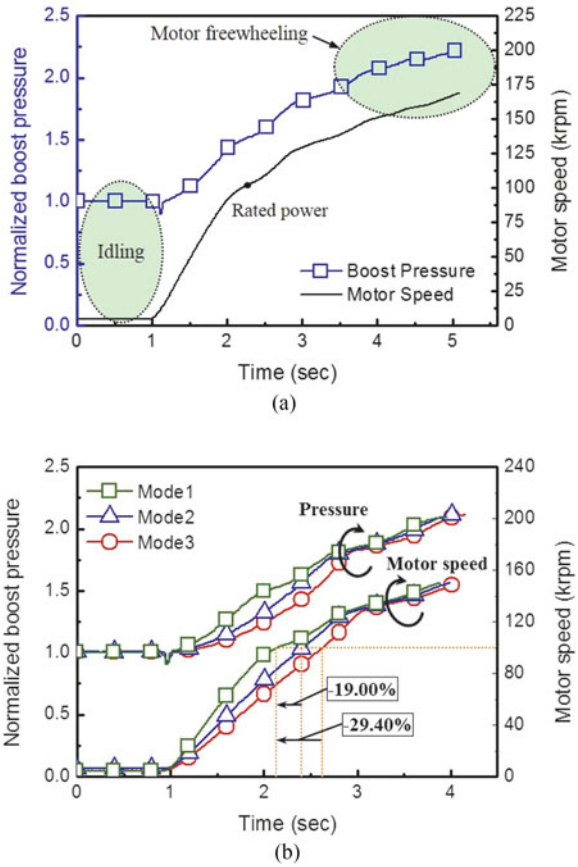


Fig. 11. Boost pressure and motor speed as the test results. (a) Operating state of electrically assisted turbocharger. (b) Comparison of the normalized pressures and motor speed according to the drive modes.

## V. EFFECTIVENESS OF DESIGNED MOTOR IN TURBOCHARGER

The research objective is to apply the designed motor to the turbocharger to verify the effect of the motor performance on the turbocharger and to verify that the supercharging performance such as the boost pressure is improved beyond that of a conventional turbocharger. The results of the boost pressure measurements presented in this study were normalized by the magnitude of the normal pressure before operation of the motor. Fig. 11(a) shows the boost pressure exerted by the electrically assisted turbocharger. Given the motor speed, the boost pressure

TABLE IV
DRIVE MODES OF THE MOTOR IN TURBOCHARGER

| Drive Conditions | Motor Torque in the Electrically Assisted Turbocharger |
|---|---|
| Mode 1 | Full torque |
| Mode 2 | 50% torque |
| Mode 3 | 33% torque |
| Mode 4 | 0% torque (conventional turbocharger) |

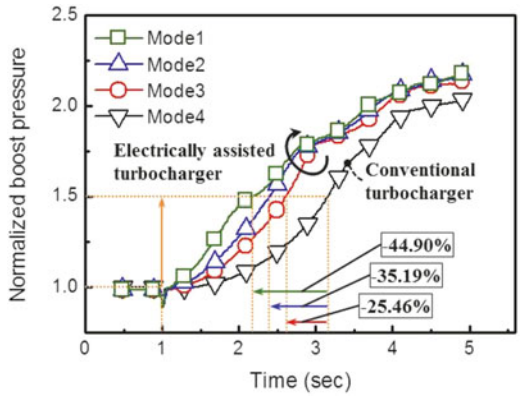


Fig. 12. Comparison of the boost pressures as the experiment results according to the drive modes.

was rapidly increased by the motor under the rated speed. Between the rated and maximum speeds, the pressure and the motor speed gradually increased due to the decreasing torque. At over 150 krpm, the motor was rotated freely by the high-speed exhaust gas. The speed characteristics of the designed motor according to the drive mode are compared in Fig. 11(b). The drive modes of the motor are shown in Table IV. The speed characteristics were analyzed up to the rated speed. As a result, the times taken to reach 100 krpm under drive mode 1 were approximately 19.0% and 29.4% faster, respectively, than under modes 2 and 3 due to the higher torque. Fig. 11(b) also presents the normalized boost pressure according to the drive modes; it is increased proportionally to the motor speed. In addition, it is shown that the boost pressure increased rapidly since the motor torque is high. Therefore, it was verified that a higher motor torque and power quickly increases the motor speed, which implies that the performance of the turbocharger can be improved [23], [24]. The boost pressure exerted by the electrically assisted turbocharger is compared with a conventional turbocharger in Fig. 12. By means of the designed motor, the pressure under modes 1, 2, and 3 increased faster than under mode 4. The time that it took to reach the 1.5 normalized boost pressure under drive modes 1–3 was faster by about 44.9%, 35.2%, and 25.5%, respectively, than under mode 4. This is important because it shows that the turbo lag can be reduced during vehicle acceleration. In addition, it was verified that a higher motor torque quickly increases the boost pressure, which means that the turbo lag elimination performance can be improved by a higher motor torque, which directly affects the acceleration of the vehicle.

In summary, through experiments, the effectiveness of the proposed design methodology for an ultra-high-speed motor

and the performance of the designed motor were verified. Furthermore, given the boost pressure of the electrically assisted turbocharger, it was verified that the performance of the turbocharger can be improved by adopting the proposed ultra-high-speed SPMSM.

## VI. Conclusion

The design of the 4-kW 150-krpm ultra-high-speed SPMSM for an electrically assisted turbocharger was presented. In the proposed design methodology, an NdFeB magnet was used to maximize the power density. Furthermore, the electromechanical undamped natural frequency and damping ratio obtained from the transfer function of the system were used to achieve a fast-speed response. Based on the results of the analysis, the appropriate series turn number per phase and axial length were determined considering the current density and cooling method. Consequently, the volume of the motor was reduced by approximately 35.0%. The rated power and speed increased by approximately 14.3%. The speed response of the improved motor was 35.1% faster than that of the prototype. Considering the inertia of the impeller and the turbine, the speed response of the improved motor was 8.6% faster than that of the prototype. Performance of the designed motor, such as the torque and speed, was verified through component tests. Finally, the effectiveness of the designed motor in the turbocharger was verified through the system experiments. As a result, the rising speed of the boost pressure exerted by the motor in the electrically assisted turbocharger was improved by about 44.9% over that of the conventional turbocharger.

## References


[1] J. R. Bumby *et al.*, "Electrical machines for use in electrically assisted turbochargers," in *Proc. IET 2nd Int. Conf. Power Electron. Mach. Drives*, Mar./Apr. 2004, vol. 1, pp. 344–349.

[2] J. Bumby, S. Crossland, and J. Carter, "Electrically assisted turbochargers: Their potential for energy recovery," in *Proc. IET Hybrid Veh. Conf.*, Dec. 2006, pp. 43–52.

[3] A. Borisavljevic, H. Polinder, and J. A. Ferreira, "On the speed limits of permanent-magnet machines," *IEEE Trans. Ind. Electron.*, vol. 57, no. 1, pp. 220–227, Jan. 2010.

[4] A. Binder, T. Schneider, and M. Klohr, "Fixation of buried and surface mounted magnets in high-speed permanent magnet synchronous motors," in *Proc. IEEE Conf. Rec. Ind. Appl.*, Oct. 2005, vol. 4, pp. 2843–2848.

[5] J. F. Gieras, "Design of permanent magnet brushless motors for high-speed applications," in *Proc. IEEE Int. Conf. Electr. Mach. Syst.*, Oct. 2014, pp. 1–16.

[6] D. Gerada, A. Mebarki, N. L. Brown, K. J. Bradley, and C. Gerada, "Design aspects of high-speed high-power laminated-rotor induction machines," *IEEE Trans. Ind. Electron.*, vol. 58, no. 9, pp. 4039–4047, Sep. 2011.

[7] J. R. Bumby, E. Spooner, and M. Jagiela, "Equivalent circuit analysis of solid-rotor induction machines with reference to turbocharger accelerator applications," *IEE Proc. Electric Power Appl.*, vol. 153, no. 1, pp. 31–39, Jan. 2006.

[8] S. De Caro, C. Scaffidi, T. Scimone, and A. Testa, "Energy balance assessment on vehicles with electrically assisted internal combustion engines," in *Proc. IEEE Int. Conf. Clean Electr. Power*, Jun. 2015, pp. 786–792.

[9] C. C. Hwang, S. S. Hung, C. T. Liu, and S. P. Cheng, "Optimal design of a high-speed SPM motor for machine tool applications," *IEEE Trans. Magn.*, vol. 50, no. 1, Jan. 2014, Art. no. 4002304.

[10] S. M. Jang, H. W. Cho, and S. K. Choi, "Design and analysis of a high-speed brushless DC motor for centrifugal compressor," *IEEE Trans. Magn.*, vol. 43, no. 6, pp. 2573–2575, Jun. 2007.

[11] N. Bianchi, S. Bolognani, and F. Luise, "Analysis and design of a PM brushless motor for high-speed operations," *IEEE Trans. Energy Convers.*, vol. 20, no. 3, pp. 629–637, Sep. 2005.

[12] M. Sridharbabu, T. Kosaka, and N. Matsui, "Design analysis and improvement high-speed hybrid excitation motor for main spindle drive in machine tools based on experimental results of prototype machine," in *Proc. IEEE 8th Int. Conf. Power Electron. ECCE Asia*, May/Jun. 2011, pp. 1935–1939.

[13] T. Schneider and A. Binder, "Design and evaluation of a 60 000 rpm permanent magnet bearingless high-speed motor," in *Proc. IEEE 7th Int. Conf. Power Electron. Drive Syst.*, pp. 1–8, Nov. 2007.

[14] P.-D. Pfister and Y. Perriard, "Very-high-speed slotless permanent-magnet motors: Analytical modeling, optimization, design, and torque measurement methods," *IEEE Trans. Ind. Electron.* vol. 57, no. 1, pp. 296–303, Jan. 2010.

[15] M. S. Lim, S. H. Chai, and J. P. Hong, "Design and verification of 150-krpm PMSM based on experiment results of prototype," *IEEE Trans. Ind. Electron.*, vol. 62, no. 12, pp. 7827–7836, Mar. 2015.

[16] J. J. Cathey, "Synchronous machines," in *Electric Machines: Analysis and Design Applying MATLAB*, 1st ed. New York, NY, USA: McGraw-Hill Science/Engineering/Math, 2000, pp. 421–515.

[17] R. C. Dorf and R. H. Bishop, "Performance of feedback control systems," in *modern control systems*, 12th ed. Upper Saddle River, NJ, USA: Pearson Education, 2011, pp. 326–407.

[18] L. Zhao *et al.*, "A highly efficient 200 000 RPM permanent magnet motor system," *IEEE Trans. Magn.* vol. 43, no. 6, pp. 2528–2530, Jun. 2007.

[19] J. R. Hendershot and T. J. E. Miller, "Basic design choices," in *Design of Brushless Permanent-Magnet Machines*, 2nd ed. Venice, FL USA: Motor Design Books LLC, 2010, pp. 65–156.

[20] J. Hur, "Characteristic analysis of interior permanent-magnet synchronous motor in electrohydraulic power steering systems," *IEEE Trans. Ind. Electron.* vol. 55, no. 6, pp. 2316–2323, Jun. 2008.

[21] B. H. Lee, S. O. Kwon, T. Sun, J. P. Hong, G. H. Lee, and J. Hur, "Modeling of core loss resistance for d-q equivalent circuit analysis of IPMSM considering harmonic linkage flux," *IEEE Trans. Magn.*, vol. 47, no. 5, pp. 1066–1069, May 2011.

[22] J. W. Kim, I. S. Jeong, G. H. Nam, J. S. Yang, and T. W. Hwang, "Sensorless control of PMSM in a high-speed region considering iron loss," *IEEE Trans. Ind. Electron.*, vol. 62, no. 10, pp. 6151–6159, Oct. 2015.

[23] B. Xu, M. Cheng, H. Yang, J. Zhang, and C. Sun, "A hybrid displacement/pressure control scheme for an electrohydraulic flow matching system," *IEEE/ASME Trans. Mechatronics*, vol. 20, no. 6, pp. 2771–2782, Dec. 2015.

[24] A. Dell'Amico and P. Krus, "Modeling, simulation, and experimental investigation of an electrohydraulic closed-center power steering system," *IEEE/ASME Trans. Mechatronics*, vol. 20, no. 5, pp. 2452–2462, Oct. 2015.

**Myung-Seop Lim** received the Bachelor's degree in mechanical engineering and the Master's degree in automotive engineering in 2012 and 2014, respectively, from Hanyang University, Seoul, Korea, where he is currently working toward the Ph.D. degree in automotive engineering.

His current research interests include electric machine design for automotive and robot applications and sensorless drive.

**Ji-Min Kim** received the Bachelor's degree in mechanical engineering in 2009 from Hanyang University, Seoul, Korea where he is currently working toward the Ph.D. degree in automotive engineering.

His current research interests include optimization, analysis, and design of electric machine and numerical analysis of electromagnetic.

**Yong-Suk Hwang** received the Bachelor's degree in mechanical engineering from Korea University, Seoul, Korea, in 2003, and the Master's degree in automotive engineering in 2012 from Hanyang University, Seoul, where he is currently working toward Ph.D. degree.

His current research interests include the development and the improvement of analysis methods for the effective design of electric machines.

**Jung-Pyo Hong** received the Ph.D. degree in electrical engineering from Hanyang University, Seoul, Korea, in 1995.

From 1996 to 2006, he was a Professor of Changwon National University, Chang-won, Korea. Since 2006, he has been a Professor with Hanyang University. His current research interests include the design of electric machines and optimization and numerical analysis of electromechanics.